






RESEARCH ARTICLE

10.1029/2025JD044332

Special Collection:

TEMPO Data Products, Science, and Applications

First Retrieval of Aerosol Vertical Profile With Passive Remote Sensing: Part 1. Development of Algorithm Theoretical Basis

Zhendong Lu¹ , Jun Wang^{1,2} , Xi Chen², Xiaoguang Xu³, Meng Zhou^{1,4}, Dejian Fu⁵, and Jonathan H. Jiang⁵ 

Key Points:

- An algorithm is developed to first derive the aerosol vertical profile from ultraviolet (UV) and O₂ absorption bands with passive remote sensing
- Major eigenvectors from the principal component analysis of 15-year aerosol profile measurements by spaceborne lidar serve as prior information
- The synthetic retrieval experiments confirm the feasibility and robustness of the new retrieval algorithm on a theoretical basis

Supporting Information:

Supporting Information may be found in the online version of this article.

Correspondence to:

Z. Lu and J. Wang,
zhendong-lu@uiowa.edu;
jun-wang-1@uiowa.edu

Citation:

Lu, Z., Wang, J., Chen, X., Xu, X., Zhou, M., Fu, D., & Jiang, J. H. (2025). First retrieval of aerosol vertical profile with passive remote sensing: Part 1. Development of algorithm theoretical basis. *Journal of Geophysical Research: Atmospheres*, 130, e2025JD044332. <https://doi.org/10.1029/2025JD044332>

Received 12 MAY 2025

Accepted 17 OCT 2025

¹Interdisciplinary Graduate Program in Informatics, The University of Iowa, Iowa City, IA, USA, ²Department of Chemical and Biochemical Engineering, Center for Global and Regional Environmental Research and Iowa Technology Institute, The University of Iowa, Iowa City, IA, USA, ³GESTAR-II and Department of Physics, University of Maryland Baltimore County, Baltimore, MD, USA, ⁴Now at GESTAR-II, University of Maryland Baltimore County, Baltimore, MD, USA, ⁵Jet Propulsion Laboratory, California Institute of Technology, Pasadena, CA, USA

Abstract This paper presents the first part of a two-part study to develop a new algorithm to retrieve the aerosol vertical extinction profile using the hyperspectral measurements at ultraviolet bands, O₂ A-band and B-band, from the Tropospheric Monitoring Instrument (TROPOMI). We represent the aerosol vertical profile by the weighted sum of 3–5 most important EOFs (empirical orthogonal function, i.e., eigenvectors) from the principal component analysis (PCA) of the 15-year record of aerosol extinction profiles from spaceborne lidar Cloud-Aerosol Lidar with Orthogonal Polarization (CALIOP). Hence, the retrieval is simplified to derive 3–5 coefficients or weights of corresponding EOFs to capture the variation of aerosol vertical profiles. A new PCA module was developed in the Unified Linearized Vector Radiative Transfer Model (UNL-VRTM) for calculating the Jacobians of top-of-atmosphere (TOA) reflectance with respect to the weights of EOFs, which is used to facilitate the optimal inversion of the EOF weights. The analytical Jacobian calculations are validated against the Jacobians computed from a finite difference method. The averaging kernel analysis for directly retrieving the aerosol extinction profiles from measurements of TROPOMI and high-resolution metagrating spectropolarimeter for aerosol profiling was provided. Finally, the retrieval experiments with synthetic TROPOMI measurements generated by UNL-VRTM were conducted to verify the self-consistency and feasibility of the inversion algorithm on a theoretical basis.

Plain Language Summary The vertical distribution of aerosols regulates the aerosol impacts on the climate, cloud formation, and surface air quality. While the remote sensing of the aerosol vertical profile from active satellite sensors suffers from the narrow swath, the passive remote sensing provides much wider spatial coverage with lower information content. This study develops a new algorithm to retrieve the aerosol vertical profile from the UV and oxygen absorption bands measured by passive satellite instruments. The major vertical variation modes of the aerosol extinction profiles are derived from the principal component analysis of 15 years of aerosol profile measurements from the spaceborne lidar Cloud-Aerosol Lidar with Orthogonal Polarization, serving as the prior information for the retrieval. Therefore, retrieving only a few weighting coefficients of these major variation modes from the passive remote sensing is sufficient to reconstruct the aerosol vertical profile. An optimal inversion method is applied for the retrieval based on the Unified Linearized Vector Radiative Transfer Model (UNL-VRTM). The theoretical feasibility and robustness of the retrieval algorithm are verified via the retrieval experiments with synthetic measurements of Tropospheric Monitoring Instrument generated by UNL-VRTM.

1. Introduction

Aerosol vertical distribution plays an important role in regulating aerosol effects on climate and air quality. First, the magnitude even the sign of the aerosol radiative effects can be regulated by the relative position of absorbing aerosols and clouds in the vertical dimension (Ge et al., 2014; Wang & Christopher, 2006; Zarzycki & Bond, 2010). Second, the vertical distribution of aerosols affects the thermodynamic structure of the atmosphere by absorbing and scattering solar and terrestrial radiation, consequently regulating the cloud formation and its lifecycle (Johnson et al., 2004; Wilcox, 2012). Third, for cloud-free conditions, the aerosol radiative effects and feedback also depend on the aerosol vertical distribution at ultraviolet (UV), visible-near infrared (Vis-NIR),

© 2025. The Author(s).

This is an open access article under the terms of the [Creative Commons Attribution License](https://creativecommons.org/licenses/by/4.0/), which permits use, distribution and reproduction in any medium, provided the original work is properly cited.

shortwave infrared, and thermal infrared bands due to the interactions between aerosol absorption and Rayleigh scattering (Herman et al., 1997; Torres et al., 1998), aerosol scattering and gas absorption (Meloni et al., 2005; Mishra et al., 2015; Zhang et al., 2013) and impacts of environmental temperature profile (Mishra et al., 2015). Finally, the aerosol vertical distribution has significant impacts on the surface air quality by affecting the amount of particulate matter pollution near the surface (Chen, Wang, et al., 2021; Seo et al., 2015) and regulating the aerosol transport (Val Martin et al., 2013; Wang et al., 2006).

The daily global and operational products of total aerosol column loading from satellite measurements have been developed over more than two decades (Hsu et al., 2004, 2013; Kaufman et al., 1997; Levy et al., 2007, 2013; Lyapustin et al., 2018; Sawyer et al., 2020), but the operational data sets of global aerosol vertical distribution from observational sources are very deficient despite the critical needs of such data sets. The ground or spaceborne lidars suffer from the small spatial coverage, although they can retrieve the aerosol extinction profile with high accuracy and fine vertical resolution. For instance, the Cloud-Aerosol Lidar with Orthogonal Polarization (CALIOP) onboard the Cloud-Aerosol Lidar and Infrared Pathfinder Satellite Observation features a narrow swath of ~90 m (Winker et al., 2009), covering only 0.2% of the global area during its repeat cycle of 16 days (Kahn et al., 2008). Passive satellite sensors cannot resolve the aerosol vertical distribution layer by layer due to the limited information contained in the passive remote sensing (Colosimo et al., 2016; Ding et al., 2016), but their spatial coverage is much wider than the active sensors. For example, Tropospheric Monitoring Instrument (TROPOMI) provides operational and global retrieval of the aerosol layer height (ALH) product (Nanda et al., 2019). However, TROPOMI operational ALH is systematically lower than the counterpart of CALIOP, which is defined as an aerosol extinction-weighted height, by ~1 km on average over ocean and more than 2 km over land (Chen, Wang, et al., 2021; Nanda et al., 2020). Furthermore, passive remote sensing techniques at present only retrieve a single effective ALH under the assumption that the aerosol profile follows a certain distribution function (e.g., quasi-Gaussian and exponential-decaying function) (Chen, Wang, et al., 2021; Lu et al., 2021, 2023; Xu et al., 2017, 2018), which may be insufficient for the cases of the multilayer structure of aerosols (Hollstein & Filipitsch, 2014). The observational data sets of aerosol vertical profiles with full spatial and temporal coverage are highly needed.

This research develops an algorithm to derive the aerosol vertical extinction profile from the hyperspectral measurements in the UV-Vis-NIR spectrum, such as TROPOMI, with a technique based on principal component analysis (PCA). It seeks to derive the aerosol extinction vertical profile instead of retrieving an effective ALH, therefore going beyond the previous studies, which deployed techniques such as O₂ (or O₂-O₂) absorption spectroscopy (Chimot et al., 2018; Xu et al., 2017, 2019), radiance-only or polarization measurements in UV or deep blue bands (Joseph et al., 2008; Lee et al., 2020; Wu et al., 2016), multiangle or polarimetric measurements in O₂ absorption bands (Chen, Wang, et al., 2021; Choi et al., 2021; Ding et al., 2016), infrared thermal techniques (Peyridieu et al., 2010; Vandenbussche et al., 2013), and stereoscopic photogrammetry (Nelson et al., 2013). Our research algorithm combines the hyperspectral measurements at UV, O₂-A, and O₂-B bands from TROPOMI with the 15-year climatology of aerosol extinction profiles from CALIOP to obtain as much information as possible. Each aerosol vertical profile is represented by a weighted sum of the 3–5 EOFs (empirical orthogonal function, i.e., eigenvectors) from the PCA of the multiyear CALIOP data. Hence, the retrieval is simplified as retrieving 3–5 weights of corresponding EOFs to capture the variation of aerosol profiles from space. The size of the state vector is reasonably small but still adequate for characterizing variations of aerosol profiles because the dominant variation features are represented by the CALIOP-based EOFs.

Section 2 introduces the radiative transfer model we used, the CALIOP data, the synthetic satellite measurements, and the theoretical basis of this study. Section 3 provides the PCA results of the multiyear CALIOP data over North Atlantic Ocean and the validation of the PCA module developed in the radiative transfer model. The averaging kernel analysis of the aerosol vertical profile retrieval is presented in Section 4. Section 5 provides the results of the retrieval experiments using the synthetic TROPOMI measurements, followed by the summary and conclusions in Section 6.

2. Models, Data Sources, and Theoretical Basis

2.1. UNL-VRTM

The radiative transfer model, Unified Linearized Vector Radiative Transfer Model (UNL-VRTM) (Wang et al., 2014) version 3.0.1, is used to simulate the top-of-atmosphere (TOA) radiance. A new PCA module has

Table 1
Spectral Configuration of Synthetic TROPOMI Measurements

Spectral range [nm]	Spectral interval [nm]	FWHM ^a [nm]	Surface reflectance
350–390 (UV)	0.195	0.550	0.03200
680–700 (O ₂ -B)	0.128	0.345	0.02044
750–780 (O ₂ -A)	0.122	0.345	0.01944

^aFWHM stands for full width at half maximum.

been developed and validated in the UNL-VRM for representing aerosol vertical profiles using first 3–5 EOFs and calculating the Jacobians of TOA reflectance with respect to the weights of most important EOF modes for aerosol vertical profiles (See Section 3.2). The optimal inversion module incorporated in the UNL-VRM will be used to do the retrieval. UNL-VRM has been successfully used in a series of past studies for aerosol retrievals and information content analysis (Ding et al., 2016; Hou et al., 2016, 2017, 2020) and ALH retrieval from passive satellite sensors (Chen, Wang, et al., 2021; Xu et al., 2017, 2019).

2.2. CALIOP Data

Monthly gridded aerosol extinction profiles at 532 nm during June 2006–December 2021 over tropical North Atlantic Ocean (60°W–0°, 0°–30°N) from CALIOP Level 3 Tropospheric Aerosol Profile product (Winker et al., 2009, 2013) are used for extracting the first five EOFs with the PCA method. CALIOP Level 3 data feature a horizontal resolution of 2° × 5° and vertical resolution of 60 m (Winker et al., 2013). Only daytime data from CALIOP are used in this study because only passive satellite measurements in daytime will be used for retrieving aerosol vertical profiles.

2.3. Synthetic TROPOMI Data

To theoretically evaluate the feasibility of the research algorithm for retrieving aerosol vertical profiles using the PCA method, we conducted the retrieval experiments using synthetic TROPOMI measurements generated by the UNL-VRM. UNL-VRM is used to emulate TROPOMI TOA reflectance measurements at UV, O₂-A, and O₂-B bands, and the uncertainties in TROPOMI measurements are considered by adding white (random) noise to the UNL-VRM outputs. The relative random noise follows the Gaussian distribution with the mean of 0 and standard deviation of 0.2%. The spectral configuration of the synthetic TROPOMI measurements is presented in Table 1. The configurations of spectral interval and full width at half maximum (FWHM) for the simulation mimic the real TROPOMI data (Babic et al., 2022). The self-closure retrieval experiments focus on the Saharan dust profile over tropical North Atlantic Ocean. The dust aerosol model was adopted from Chen, Wang, et al. (2021), and the aerosol optical properties including the Ångström exponent are assumed to be vertically invariant. Therefore, the shapes of the normalized aerosol extinction profiles are identical at different wavelengths from UV to NIR. The surface reflectance of the open ocean water at visible and near-infrared range is adopted from the ASTER spectral library (Baldrige et al., 2009), while at UV channels (350–390 nm) is assumed as 0.032 (Vasilkov et al., 2019). We also generated the synthetic TROPOMI measurements for the averaging kernel analysis of smoke aerosol extinction profile retrieval over North America. The spectral configuration follows Table 1 except that the land surface reflectances were adopted from the TROPOMI surface Lambertian-equivalent reflectivity (LER) database (Tilstra et al., 2024). The surface reflectance spectrum was derived by the interpolation of TROPOMI LER at 21 wavelengths from UV to NIR channels.

2.4. Synthetic HiMAP Data

The high-resolution metagrating spectropolarimeter for aerosol profiling (HiMAP) is a spaceborne instrument concept, whose technology demonstration unit is being built at the Jet Propulsion Laboratory using NASA Earth Science Technology Office Instrument Incubator Program (IIP). By design, it will enable the aerosol vertical profiling via the hyperspectral radiance and polarimetric measurements at 680–780 nm at three viewing angles (0, ±57°) along its flight path with a swath width of 800 km across its satellite ground path at a low earth orbit of ~700 km above surface. HiMAP uses a disruptive metagrating technology to enable three functionalities within a single device: simultaneous quantification of linear polarization, spectral light dispersion, and wide swath

imaging, providing a cost-effective solution for a space-based aerosol 3-D mapping system (Hsiao et al., 2022; Richter et al., 2019). It features a high spectral resolving power of 4,300 and a signal-to-noise ratio of 300. The uncertainty of the degree of linear polarization (DoLP) from HiMAP measurements is within 0.5% (Hsiao et al., 2022). We generated the synthetic full-Stokes measurements for HiMAP using UNL-VRM with the spectral interval of 0.085 nm and FWHM of 0.180 nm at three viewing zenith angles (0° , $\pm 57^\circ$) at O₂-A (750–780 nm) and O₂-B (680–700 nm) bands. The land surface reflectance spectrum for the synthetic HiMAP data is also derived from the TROPOMI surface LER database (Tilstra et al., 2024) by linear interpolation with the assumption of the Lambertian surface. The synthetic HiMAP measurements are used to conduct the averaging kernel analysis and synthetic retrieval of aerosol extinction profile without the PCA technique to demonstrate the advantage of the proposed PCA technique for retrieving the aerosol vertical profile (Section 4).

2.5. Representing Aerosol Profiles by EOFs

While the aerosol profile varies day by day, the physical processes regulating the aerosol profiles are limited, including the boundary layer process, convection and injection process and long-range transport. Therefore, the variation of aerosol profiles is a result of the change of relative importance of these processes. Reid et al. (2017) shows that the EOFs from the PCA of lidar extinction profiles represent independent variation features at different altitudes. Consequently, the weighted sum of first several EOFs can reconstruct the shape of the aerosol profile.

$$\beta_{\text{ext}}(z) = \tau_0 \left(\sum_{i=1}^n w_i E_i(z) + \overline{\beta_{\text{ext}}}(z) \right) \quad (1)$$

where β_{ext} is the aerosol extinction coefficient as a function of altitude z , τ_0 is the aerosol optical depth (AOD), E_i and w_i are the i th EOF and corresponding weight, and $\overline{\beta_{\text{ext}}}$ is the mean of an ensemble of multiyear aerosol normalized vertical extinction profiles, $\beta_{\text{ext},N}$, in which each element is the CALIOP aerosol extinction profile normalized by its AOD. The EOFs are the eigenvectors from the PCA of $\beta_{\text{ext},N}$, while the weights of EOF are the corresponding elements of so-called principal components (PCs).

2.6. Optimal Inversion and Averaging Kernel Analysis

The state vector x to be retrieved includes 3–5 weights of most important EOFs. Based on the optimal estimation theory (Rodgers, 2000) and L-BFGS-B algorithm (Byrd et al., 1995; Xiao & Zhang, 2008), the optimal inversion of the retrieved parameters seeks to minimize the cost function by iteratively calculating the Jacobian matrix and adjusting the state vector estimation. The cost function $J(x)$ in this study is defined as

$$J(x) = \frac{1}{2} [F(x) - y]^T S_\epsilon^{-1} [F(x) - y] + \frac{1}{2} \gamma (x - x_a)^T S_a^{-1} (x - x_a) \quad (2)$$

where $F(x)$ is the radiative transfer model, y is the measurement vector comprising observed TOA radiances by satellite sensors at the oxygen absorption spectrum, x_a is the priori estimate for x and can be the mean of the aerosol extinction profile from the CALIOP climatology by region and season, γ is the regularization factor to balance the fitting error versus the penalty error, and S_ϵ and S_a are the covariance matrices of the measurement error and priori error.

The critical part of the optimal inversion is calculating the Jacobian matrix K .

$$K = \frac{\partial F(x)}{\partial x} = \frac{\partial I}{\partial x} \quad (3)$$

here, I is the forward-model computed vector of TOA radiances at different wavelengths. The Jacobian of I with respect to the EOF weights w can be computed based on the chain rule and Equation 1.

$$\frac{\partial I}{\partial w} = \frac{\partial I}{\partial \beta_{\text{ext}}} \frac{\partial \beta_{\text{ext}}}{\partial w} = \frac{\partial I}{\partial \beta_{\text{ext}}} \tau_0 E \quad (4)$$

where β_{ext} is the vector containing the aerosol extinction coefficient at each vertical layer.

The DoLP in the principal plane can be computed as Equation 5.

$$\text{DoLP} = -\frac{Q}{I} \quad (5)$$

here, Q is the Stokes vector component representing the linear polarization. The Jacobian of DoLP with respect to the EOF weights can be derived as Equation 6.

$$\frac{\partial \text{DoLP}}{\partial w} = \left(\frac{Q}{I^2} \frac{\partial I}{\partial \beta_{\text{ext}}} - \frac{1}{I} \frac{\partial Q}{\partial \beta_{\text{ext}}} \right) \tau_0 E \quad (6)$$

The Jacobian of I and Q with respect to β_{ext} is already implemented in the UNL-VRM.

The averaging kernel matrix A is computed as

$$A = \frac{\partial \hat{x}}{\partial x} = (K^T S_{\epsilon}^{-1} K + S_a^{-1})^{-1} K^T S_{\epsilon}^{-1} K \quad (7)$$

here, \hat{x} is the estimate (retrieval) of the state vector. The trace of A is called the degree of freedom for signal (DFS), which indicates the information amount that can be retrieved from the satellite measurements.

3. Development of PC-Based Module for Aerosol Vertical Profile in UNL-VRM

3.1. PCA of CALIOP Vertical Profiles

PCA is a useful tool to analyze the independent variation modes of aerosol vertical distribution and reveal the altitude ranges of major physical processes affecting aerosol vertical distribution (Chew et al., 2013; Reid et al., 2017). Our previous work successfully applied PCA to CALIOP aerosol extinction profiles over the tropical North Atlantic Ocean to identify the variation modes representing dust transport and the marine boundary layer process (Lu et al., 2023). In this study, we used CALIOP aerosol extinction profiles again as an example to develop the theoretical framework. We conducted PCA of 532-nm aerosol extinction profiles from the daytime CALIOP Level 3 product over the tropical North Atlantic Ocean (60°W–0°, 0°–30°N) during June 2006–December 2021. Different from Lu et al. (2023), to decouple the shape and the column loading of the aerosol vertical profiles, the normalized aerosol extinction profiles by their AOD were used as the inputs for PCA so that the EOFs only represent the variation features of the aerosol profile shapes. Figure 1 presents the PCA results of the aerosol vertical profile shapes from the CALIOP daytime product. The first three EOFs can explain 70% of the total variance of the aerosol profile shapes over the tropical North Atlantic. The correlations between PCs and normalized extinction profiles indicate that the variations of dust transport at 2–5 km are represented by EOF 1–4 at different altitudes, and the majority of the variability of the marine boundary layer process below 2 km is accounted for by EOF 1. Figure 1 attests the conjecture that once the EOFs are derived from the CALIOP climatology, only the first 3–5 weights of the corresponding EOFs need to be retrieved from satellite measurements to recover a single aerosol profile. While results in Figure 1 are for the ocean only, PCA in our algorithm can be applied regionally, accounting for local aerosol types and physical processes. Figure S1 in Supporting Information S1 displays the PCA results over the Western United States using 15 years of the CALIOP Level 3 product, showing the similar findings that the vertical variation of aerosol extinction can be explained overwhelmingly by 3–5 EOFs.

3.2. New PC Module for Aerosol Vertical Profile in the UNL-VRM

We developed a new PC module in the UNL-VRM for representing the aerosol vertical profile using the precalculated EOFs and their corresponding weights in the model. To expedite the computation and match the vertical coordinate of the GEOS-Chem model, we aggregated the CALIOP aerosol extinction profiles to 47 hybrid sigma-pressure layers of GEOS-Chem and then computed the first three EOFs via PCA. UNL-VRM is subsequently set up for those 47 layers. To evaluate the fidelity of representing aerosol profiles using the PCA method in the UNL-VRM, we picked three aerosol profile samples with elevated dust transport at 2–5 km and

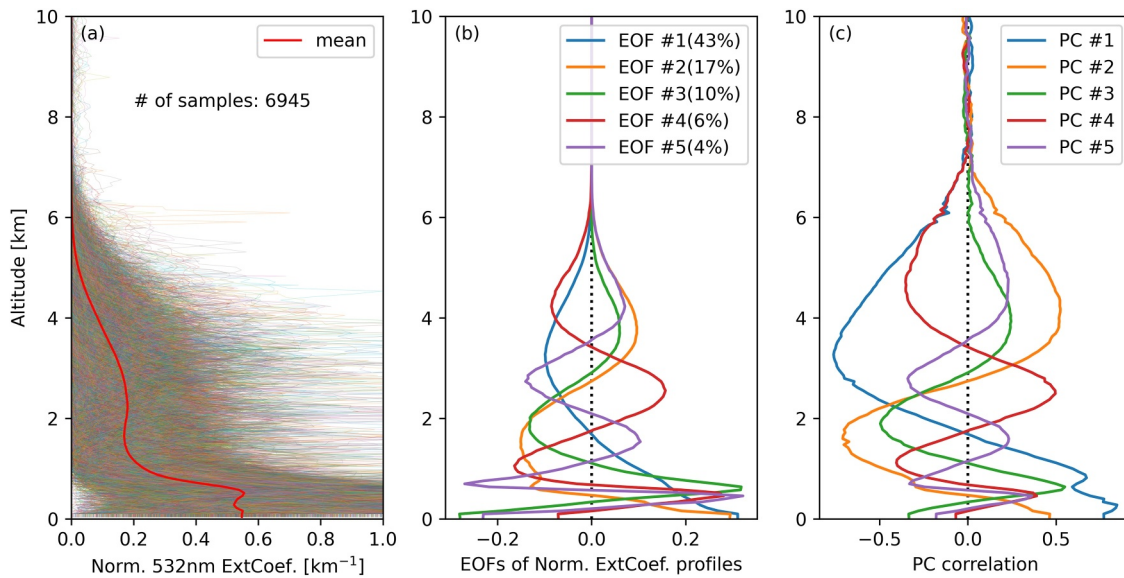


Figure 1. Principal component analysis results for normalized daytime aerosol profiles by aerosol optical depth over the tropical North Atlantic Ocean (60°W–0°, 0°–30°N) using 15 years (June 2006–December 2021) of Cloud-Aerosol Lidar with Orthogonal Polarization (CALIOP) Level 3 product. (a) All the normalized aerosol profiles from CALIOP. (b) The first five EOF modes. (c) The correlation coefficients between the first five principal components and the normalized aerosol extinction coefficients in the sample data at each vertical layer.

reconstructed them with the first three EOF modes at the 47 GEOS-Chem levels (Figure 2). These three profiles exhibit distinct shape characteristics. The aerosol profile shown in Figure 2b is dominated by a surface aerosol layer, with a small amount of dust aerosols present at around 2 km. The aerosol profiles displayed in Figures 2c and 2d feature surface aerosol layers within well-mixed marine boundary layers below 1 km and elevated dust layers at 2–5 km, such that there are double prominent layers in both aerosol profiles. The reconstruction of the three aerosol extinction profiles with only three EOFs by the PCA module in the UNL-VRM can capture the

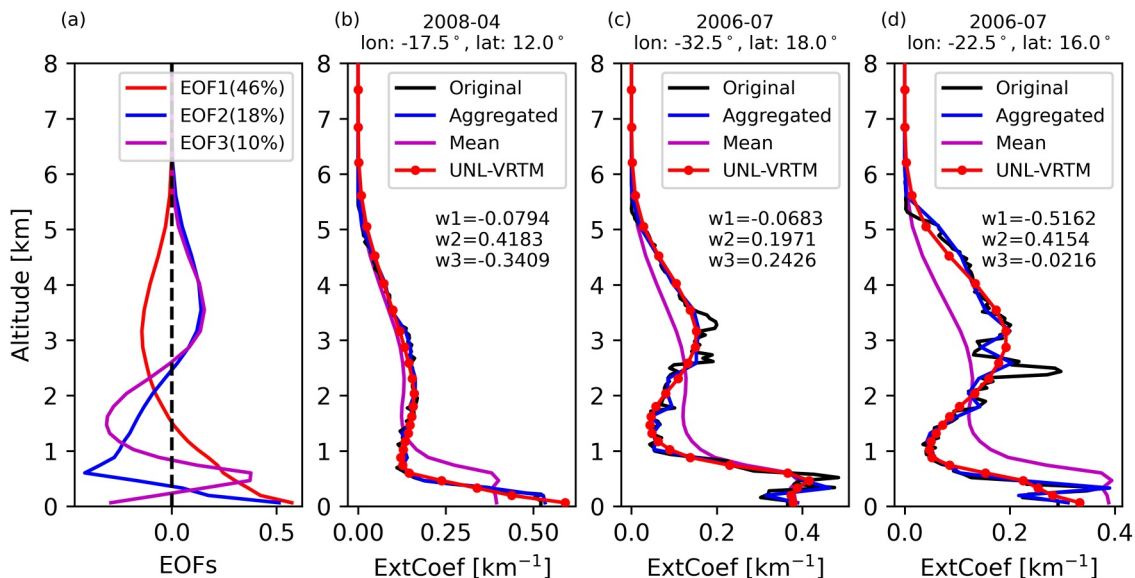


Figure 2. Examples of representing Saharan dust profiles using principal component analysis. (a) The first three EOFs from aggregated Cloud-Aerosol Lidar with Orthogonal Polarization (CALIOP) aerosol extinction profiles. (b) Aerosol extinction profile at 532 nm in April 2008 at 17.5°W, 12.0°N from original (black line, 60-m resolution) and aggregated (blue dot line, GEOS-Chem vertical coordinate) CALIOP data. Pink line shows the mean shape of all dust profiles. Red dot line is the reconstruction in Unified Linearized Vector Radiative Transfer Model at 47 GEOS-Chem hybrid pressure-sigma layers using the first three EOFs. (c) Same as (b) but for July 2006 at 32.5°W, 18.0°N. (d) Same as (b) but for July 2006 at 22.5°W, 16.0°N.

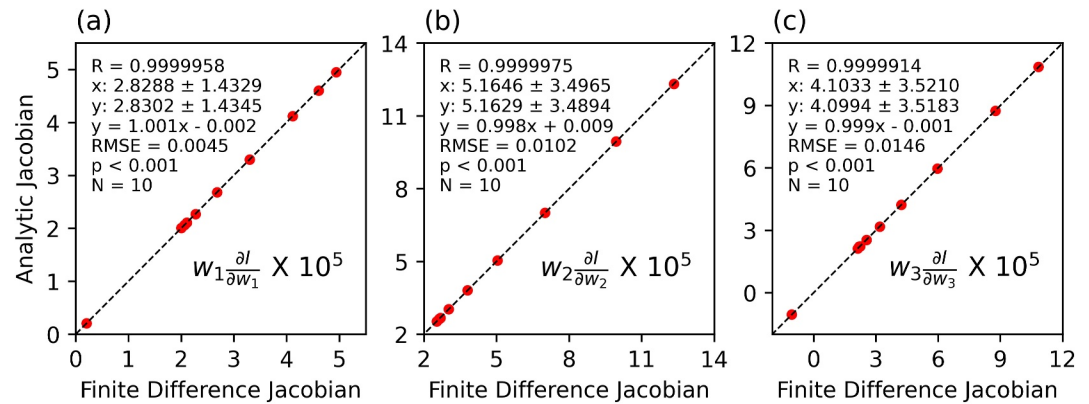


Figure 3. Comparison between analytic Jacobians calculated by Unified Linearized Vector Radiative Transfer Model and Jacobians from the finite difference method for 10 viewing geometries. Panels (a–c) show the Jacobians of TOA radiance with respect to the first three EOF weights, w_1 , w_2 , and w_3 , respectively.

most vertical variations, displaying a much better agreement with the original CALIOP aerosol profiles than the mean profile shape. The correlation coefficients between the reconstructed profiles and the aggregated CALIOP profiles are no lower than 0.94 for these three cases. This result provides us with the confidence on the fidelity of representing aerosol profiles using PCA. It also illustrates the advantage of PCA technique in capturing the multilayer structure of the aerosol profile (Figures 2c and 2d), which can never be represented by simple aerosol profile assumptions used in previous studies (Chimot et al., 2018; Xu et al., 2019; Zeng et al., 2020).

Following the theoretical basis in Section 2.5, the newly developed PC module in the UNL-VRTM is equipped with the capability of calculating the Jacobians of TOA radiances with respect to the weights of corresponding EOFs (Equation 4) in preparation of the optimal inversion. The analytical calculation of Jacobians is validated against that using the central finite difference method (Figure 3). For this validation, the weights of first three EOFs are -0.068340 , 0.197063 , and 0.242580 . The calculation is conducted at the O₂ A-band (764.0 nm) for 10 different viewing geometries. Figure 3 shows the analytic Jacobians for three EOF weights in the state vector have good agreements with those from the finite difference estimate. This result indicates that the UNL-VRTM can correctly calculate the Jacobians of TOA radiance with respect to EOF weights, which lays a solid foundation for the optimal inversion of the state vector.

4. Averaging Kernel Analysis of Aerosol Profile Retrieval

To demonstrate the advantage of the proposed PCA technique for retrieving the aerosol vertical profile, we applied a synthetic retrieval to the aerosol extinction profiles using synthetic TROPOMI and HiMAP measurements without the PCA technique for a case study. The state vector is then composed of the aerosol extinction coefficient at each vertical layer. The synthetic retrieval of the state vector \hat{x} is calculated following Equation 8 (Rodgers, 2000; Worden et al., 2007).

$$\hat{x} = x_a + A(x - x_a) \quad (8)$$

x_a and x are the a priori and ground truth of the aerosol extinction profile. A is the averaging kernel matrix (Equation 7). Averaging kernel represents the sensitivity of retrieval to the true value of the state vector. A value of one in the averaging kernel indicates a perfect retrieval in theory. The trace of averaging kernel is called the degree of freedom, which indicates the information amount that can be retrieved from the satellite measurements. Both radiance and polarimetric measurements at 680–780 nm from three viewing zenith angles (0° , $\pm 57^\circ$) are used for the synthetic HiMAP retrieval. For TROPOMI, only radiance measurements at 680–780 nm at the single viewing zenith angle of 0° are used. The solar zenith angle is assumed to be 25° for both TROPOMI and HiMAP retrievals. Table 2 presents the detailed configurations of synthetic retrievals for TROPOMI and HiMAP.

Figure 4 presents the averaging kernel calculations for retrieving the aerosol extinction coefficient at each vertical layer over North America. The meridional mean aerosol profile at the longitude of 117.5°W from 36° to 70°N

Table 2
Configurations of Synthetic Retrievals for TROPOMI and HiMAP

	HiMAP	TROPOMI
State Vector	Aerosol extinction coefficient at each vertical layer	
Measurements	Radiance and polarimetric measurements from three viewing angles	Radiance from one single viewing angle
Spectral Range [nm]	680–780	
Spectral Interval [nm]	0.085	0.122
FWHM [nm]	0.180	0.345
Surface Reflectance	TROPOMI surface LER database (Tilstra et al., 2024)	
Aerosol Model	Smoke model from Chen, Wang, et al. (2021)	
Prior Uncertainty	50%	
Measurement Uncertainty	2% for radiance; 0.005 for polarimetric measurements	2%
Model Error	5% for radiance, 0.01 for polarimetric measurements	5%
Solar Zenith Angle	25°	
Viewing Zenith Angle	0°, ±57°	0°
Relative Azimuth Angle	0°	

from CALIOP Level 3 monthly aerosol extinction profiles in August 2018 was served as the input aerosol profile for the calculations (Figure 4a). Figures 4b and 4c show the averaging kernel matrices derived from TROPOMI and HiMAP measurements, respectively. The vertical coordinate applied in this calculation is the 47 hybrid sigma-pressure layers of GEOS-Chem. Each curve in Figures 4b and 4c is one row of the averaging kernel matrix, representing the sensitivity of the retrieval at one certain layer to the true value of each vertical layer. The

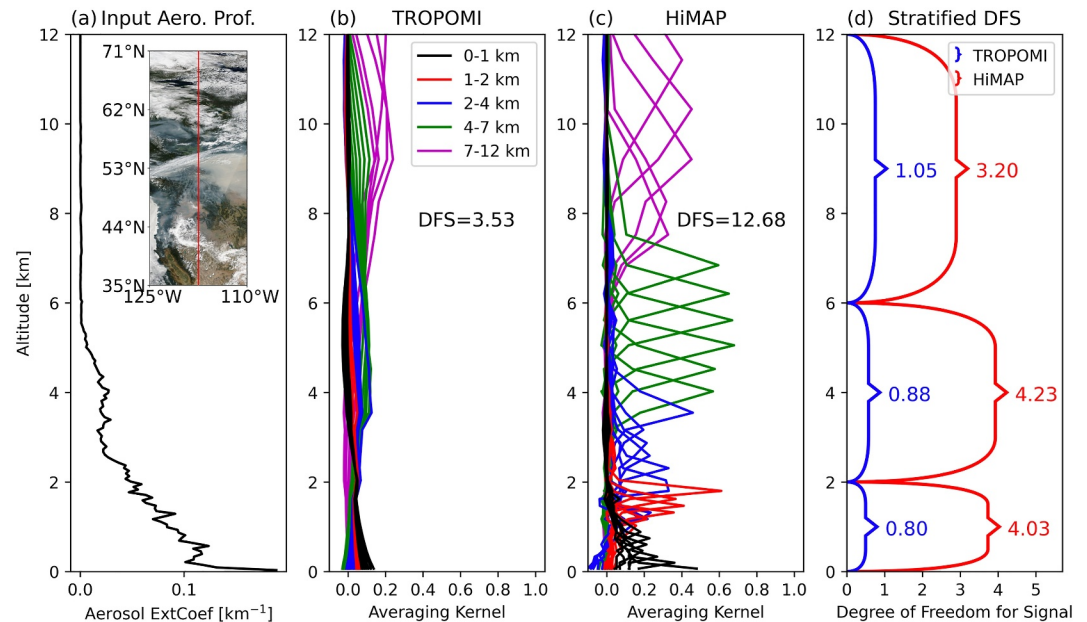


Figure 4. An example of averaging kernel calculations for retrieving the aerosol extinction coefficient at each vertical layer over North America. (a) The input aerosol extinction profile calculated from the meridional mean of Cloud-Aerosol Lidar with Orthogonal Polarization Level 3 monthly aerosol extinction profiles in Aug. 2018 at the longitude of 117.5°W from 36°N to 70°N. The inset panel is the true color image from Moderate Resolution Imaging Spectroradiometer/Terra on 15 August 2018, over North America. The red line marks the longitude of 117.5°W. (b) Averaging kernel derived from TROPOMI measurements. (c) Same as (b) but for high-resolution metagrating spectropolarimeter for aerosol profiling measurements. (d) Stratified degree of freedom for signal (DFS) of (b) and (c) for three altitude ranges of the boundary layer (0–2 km), lower free troposphere (2–6 km) and upper free troposphere (6–12 km) represented by the braces. The vertical span of each brace corresponds to the altitude range, and horizontal extent represents the DFS values for a given altitude layer.

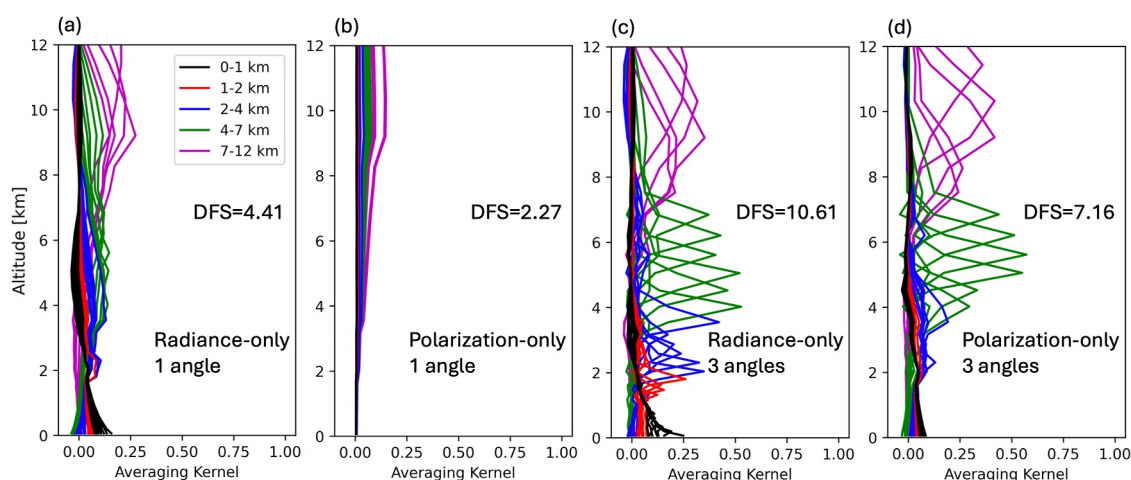


Figure 5. Averaging kernels derived from high-resolution metagrating spectropolarimeter for aerosol profiling (a) radiance-only measurements at one viewing angle (0°), (b) polarization-only measurements at one viewing angle (0°), (c) radiance-only measurements at three viewing angles, and (d) polarization-only measurements at three viewing angles.

averaging kernel values for TROPOMI are generally lower than 0.2, which indicates TROPOMI measurements cannot resolve the aerosol extinction at each vertical layer. The diagonal values of the averaging kernel matrix for HiMAP vary from 0.16 to 0.61 below 2 km, shifting to around 0.20–0.46 at 2–4 km. The values reach the peak of 0.57–0.68 at 4–7 km, then decrease to 0.32–0.45 above 7 km. The total DFS values are 3.47 and 12.68 with 47 layers in total for TROPOMI and HiMAP retrievals, respectively. Figure 4d displays the stratified DFS of TROPOMI and HiMAP retrievals at three altitude ranges: boundary layer (0–2 km), lower free troposphere (2–6 km), and upper free troposphere (6–12 km). The stratified DFS is close to 1 across all three altitude ranges for TROPOMI retrievals. In contrast, HiMAP achieves a DFS of around 4 in both the boundary layer and lower free troposphere, decreasing to around 3 in the upper free troposphere. While DFS of TROPOMI is insufficient to recover aerosol extinction at each layer in the lower part of the atmosphere, DFS of HiMAP clearly shows its greater capability to derive aerosol extinction in the lower atmosphere. The maximum diagonal averaging kernel value of HiMAP is ~ 0.7 at ~ 5 km, where the HiMAP measurements are most sensitive to.

The DFS of HiMAP is significantly larger than that of TROPOMI because of the following reasons: (a) the spectral resolution of HiMAP is roughly twice as fine as that of TROPOMI; (b) HiMAP employs three viewing angles, in contrast to TROPOMI's single-angle observation geometry; and (c) the polarimetric measurements from HiMAP add additional information content, while TROPOMI relies on radiance-only measurements. To further investigate the critical factor contributing to the larger DFS from HiMAP compared to TROPOMI, we calculated averaging kernels for various measurement configurations from HiMAP (Figure 5). Figure 5a displays the averaging kernel derived from HiMAP radiance-only measurements at a single viewing angle (0°). The DFS value is larger than that of TROPOMI (Figure 4b) by 0.94, which is solely contributed by the higher spectral resolution of HiMAP compared to TROPOMI. The DFS from HiMAP polarization-only measurements at a single viewing angle (Figure 5b) is lower than TROPOMI DFS. Figures 5c and 5d present the averaging kernels from HiMAP radiance-only and polarization-only measurements at three viewing angles. The DFS values increase by 6.20 and 4.89 compared to the corresponding single-angle configurations, which is larger than the contribution from the high spectral resolution and the polarimetric measurements. As shown in Figure 5 and previous study by Choi et al. (2021), combining the high-spectral resolution and polarization measurements at multiviewing angles is the key to enhance the measurement sensitivity of HiMAP for quantifying the atmospheric aerosol vertical distribution, since the sensitivity of the radiance measurement at single viewing from TROPOMI is not sufficient to achieve this. Depending on the scientific application needs, the sensitivity of HiMAP measurements could be further enhanced by adding measurements via its programmable gimbal system over the special regional of interests. For example, the system could expand from the current three viewing zenith angles (0° , $\pm 57^\circ$) to 9 angles (0° , $\pm 29^\circ$, $\pm 48^\circ$, $\pm 59^\circ$, and $\pm 66^\circ$) of Multi-Angle Imager for Aerosols (MAIA) (Diner et al., 2018) with a cost of reduced spatial coverage along the satellite ground track, without changing the system hardware.

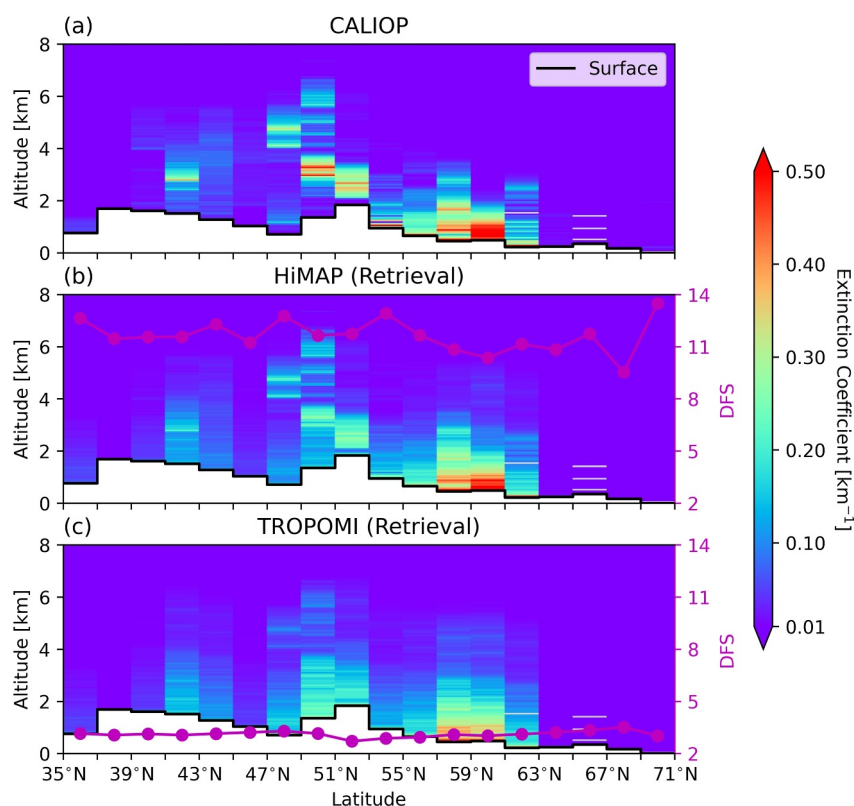


Figure 6. Synthetic retrieval of the aerosol extinction profiles using synthetic high-resolution metagrating spectropolarimeter for aerosol profiling (HiMAP) and TROPOMI measurements. (a) Cloud-Aerosol Lidar with Orthogonal Polarization Level 3 meridional aerosol extinction profile in August 2018 at the longitude of 117.5°W, served as ground truth. (b) Synthetic retrieval of (a) using both radiance and polarimetric measurements from HiMAP at 680–780 nm from 3 viewing zenith angles (0°, ±57°). The total aerosol optical depth is assumed to be perfectly retrieved. The red dot curve represents the total degree of freedom for signal for each latitude bin in reference to the vertical coordinate on the right. (c) Same as (b) but using TROPOMI radiance-only measurements at 680–780 nm.

Figure 6 displays the synthetic estimate of the aerosol extinction profiles using HiMAP and TROPOMI measurements. The total AOD is assumed to be perfectly retrieved. CALIOP Level 3 monthly meridional aerosol extinction profiles in Aug. 2018 at the longitude of 117.5°W from 36° to 70°N are used as the ground truth (Figure 6a), and the meridional average from 36° to 70°N is the a priori for the synthetic retrieval. The study domain is marked by the red line in the inset panel of Figure 4a. With the polarimetric and multiangle measurements at O₂-A and O₂-B bands with a fine spectral resolution of ~0.18 nm, HiMAP captures the primary aerosol vertical variations and spatial gradient along the satellite ground track, as shown in Figure 6b. As expected, some aerosol loading features of CALIOP's measurements are not fully recovered by HiMAP measurements, such as the aerosol extinction peak at 3–4 km at 50°N, and the aerosol extinction is overestimated in the boundary layer at 50°N. It indicates that the vertical resolution of HiMAP is coarser than that of CALIOP, though HiMAP's vertical sensitivity and resolution are much higher than the current existing passive remote sensing instruments such as TROPOMI, MicroCarb, SPEXone, Tropospheric Emissions: Monitoring of Pollution (TEMPO), Orbiting Carbon Observatory-2/3 (OCO-2/3), and Earth Polychromatic Imaging Camera (Choi et al., 2021). Owing to its enhanced measurement sensitivity similar to CALIOP, and its wide spatial coverage, which is about 800 times broader than CALIOP, HiMAP could be a unique observation system aboard satellites or airplanes to distinguish local and nonlocal pollution, advancing our understanding of the impacts of aerosols on the stability and development of planetary boundary layer (Su et al., 2022), human health, and economic prosperity (Chen, Xu, et al., 2021; Choi et al., 2021; Diner et al., 2018; Hsiao et al., 2022). TROPOMI lacks sufficient sensitivity to capture most of the aerosol vertical variations in the direct retrieval of the aerosol extinction at each vertical layer (Figures 4b and 4d), because TROPOMI does not have polarimetric and multiangle measurements and features a coarser spectral resolution than HiMAP. The total DFS for each latitude bin is marked by the red dot

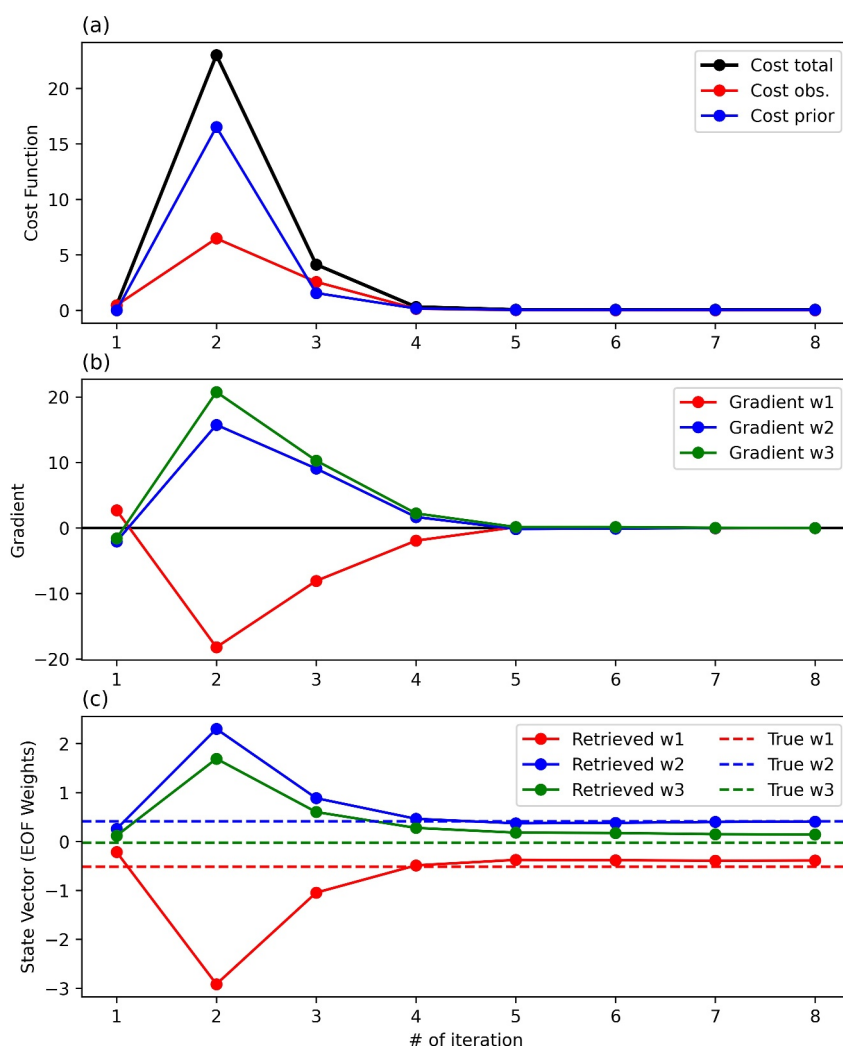


Figure 7. Iterative retrieval process for retrieving the Saharan dust profile in Figure 2(d) using synthetic TROPOMI measurements. (a) Observational term (red line), prior term (blue line), and total (black line) cost function as a function of iteration number. (b) Gradient of the cost function with respect to the state vector as a function of the iteration number. (c) The retrieved (solid line) state vector and ground truth (dashed line) as a function of the iteration number.

curves in Figures 6b and 6c in reference to the vertical coordinate on the right of each panel for HiMAP and TROPOMI retrievals, respectively. The DFS ranges from around 9 to 14 for HiMAP retrievals, while it remains much lower at around 3–4 for TROPOMI. This result indicates the method of retrieving aerosol extinction directly layer by layer using TROPOMI measurements is not feasible. We plan to integrate and test the HiMAP system using the financial supports from National Aeronautics and Space Administration (NASA) IIP in 2025–2028. When HiMAP measurements are available in the future, we will apply this PCA-based retrieval algorithm to retrieve aerosol extinction profiles by combining both HiMAP measurements and a priori information. Prior to that, TROPOMI measurements is one of the most advanced passive satellite measurements that are available for aerosol profile retrieval. The PCA technique proposed by this study, which leverages CALIOP's long-term extinction profile data sets as prior information, is necessary for a reasonable retrieval of the aerosol extinction profile (See Section 5).

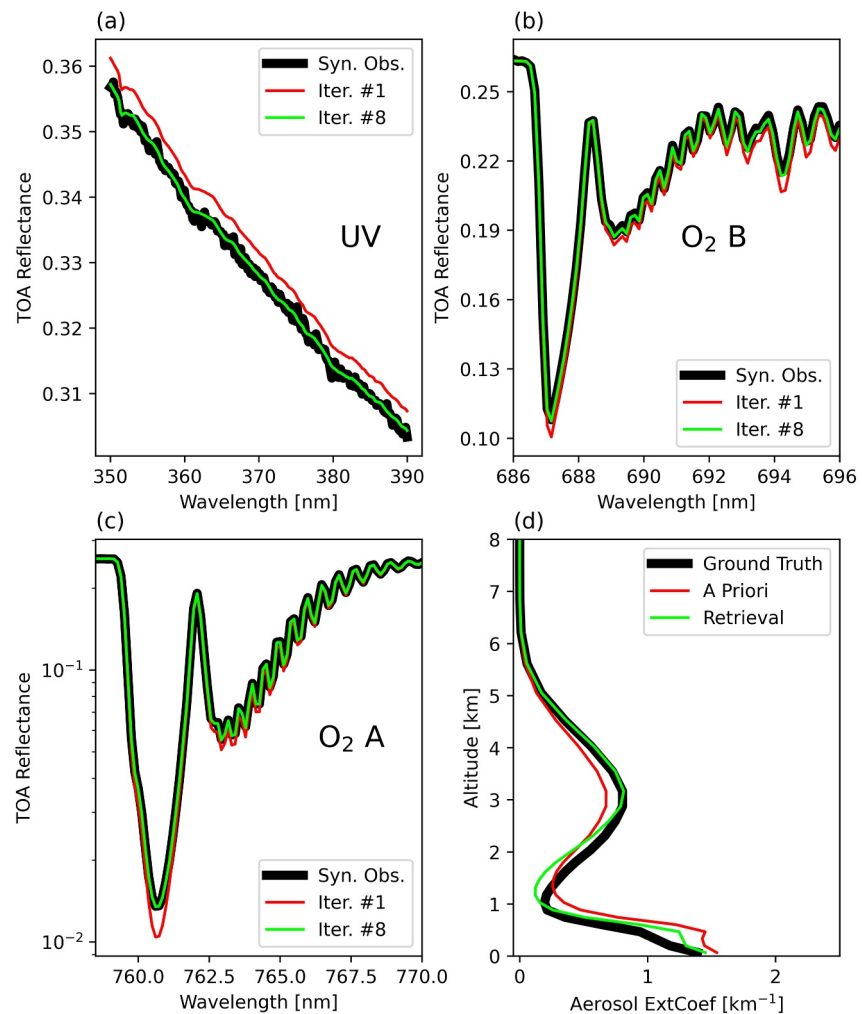


Figure 8. Spectral fitting and retrieval results for retrieving the Saharan dust profile in Figure 2(d) with the aerosol optical depth of 3.0 using synthetic TROPOMI measurements. (a) Synthetic TROPOMI observation (wide black line), simulated spectra at 1st iteration (a priori, red line) and eighth iteration (converged, green line) of TOA reflectance at ultraviolet bands. Random noise was added to the synthetic observation. (b) Same as (a) but for the O₂ B-band. (c) Same as (a) but for the O₂ A-band. (d) Ground truth (wide black line), a priori (red line), and final retrieval (green line) of the dust extinction profile.

5. Retrieving Aerosol Extinction Profile Using Synthetic Measurements With PCA

5.1. Retrieval Experiment for a Saharan Dust Profile

We implemented the retrieval experiments for Saharan dust extinction profiles using synthetic TROPOMI measurements with the PCA technique. To demonstrate the retrieval process, we selected the Saharan dust profile from the CALIOP Level 3 product in July 2006 at 22.5°W, 16.0°N (Figure 2d) as an example. The 15-year mean of the PC values (See Section 3.1) for each month and each CALIOP Level 3 pixel is used as the a priori of the state vector (i.e., three weight coefficients of EOF) for the retrievals. The a priori of the state vector for the case we selected is (−0.2164, 0.2567, 0.1181). The solar zenith angle, viewing zenith angle, and relative azimuth angle are 24°, 43°, and 0°, respectively. The AOD value at 680 nm is assumed to be 3.0 for this case. Figure 7 displays the iterative retrieval process for this case. The spectral fitting gets converged at the eighth iteration. The cost function is significantly reduced from 0.459 at the 1st iteration to 0.054 at the last iteration. The observational and prior terms of the cost function at the last iteration are 0.012 and 0.042, respectively. The absolute values of the gradient of cost function with respect to the state vector also decreases from values larger than 1.5 to that lower than 0.03. At the final iteration, the retrieved first two EOF weights (w_1 and w_2), that is, the two most important EOF weights, are getting much closer to the ground truth. From the a priori to the final retrievals, the relative

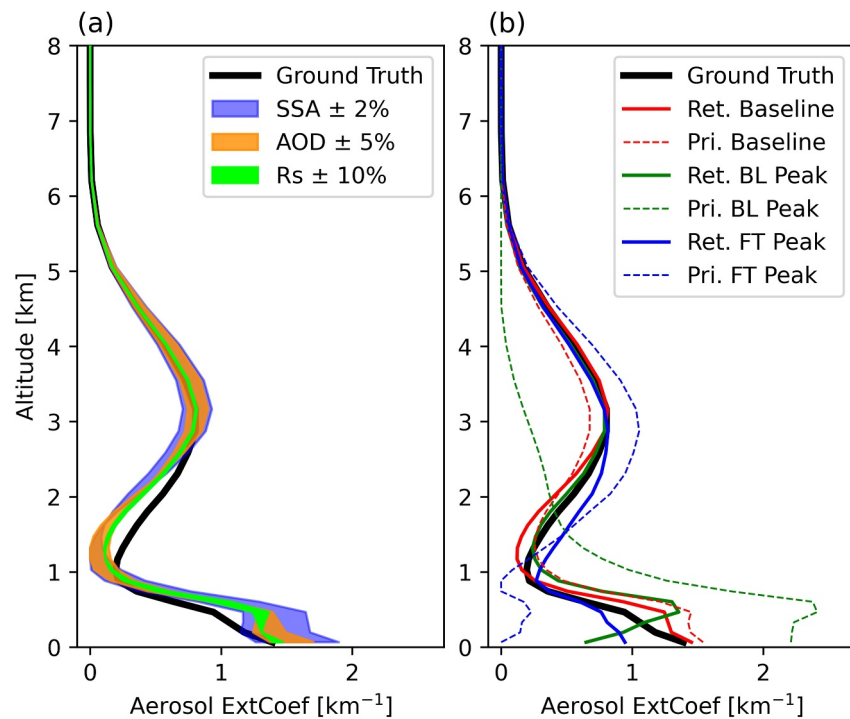


Figure 9. Error propagation analysis of retrieving the aerosol extinction profile with the principal component analysis technique for the Saharan dust case used in Section 5.1. (a) The impacts of uncertainty of single scattering albedo (SSA), aerosol optical depth (AOD), and surface reflectance on the retrieval. The blue, orange, and green shadows represent the retrieved profiles with the SSA, AOD, and surface reflectance perturbed by $\pm 2\%$, $\pm 5\%$, and $\pm 10\%$, respectively. (b) The impacts of uncertainty of a priori on the retrieval. The dashed lines with different colors are different prior profiles used in the retrievals. The solid lines are final retrievals for the corresponding a priori with the same color. See more details in the text.

differences between the estimated EOF weights and the ground truth decreased from 58.1% to 24.8% for w_1 and from 38.2% to 2.3% for w_2 . The retrieval of w_3 did not improve the estimation of w_3 significantly compared to the prior value, but it is the most insignificant one in the reconstruction of the aerosol extinction profile.

Figure 8 presents the spectral fitting result and retrieved dust profile for the selected case. The TOA reflectance of final iteration matches the synthetic TROPOMI spectra much better than that of the 1st iteration at UV, O₂ A, and O₂ B bands. The prior dust extinction profile already captures the general shape of the ground truth with the elevated dust transport peaking at around 3 km and another aerosol layer within the marine boundary layer. However, the extinction peak in the free troposphere is underestimated by the prior profile, while the peak in the boundary layer is overestimated compared to the ground truth. The final retrieval of the dust profile significantly improves the agreement with the ground truth for both extinction peaks at ~ 3 km and near the surface. The correlation coefficients between the estimated aerosol extinction and the ground truth across all vertical layers below 6 km is increased from 0.891 to 0.964 from the a priori to the final retrieval, while the root mean square error decreased from 0.225 km^{-1} to 0.132 km^{-1} .

5.2. Error Propagation Analysis

We investigated the error propagation of the uncertainties in the assumptions of single scattering albedo (SSA), AOD, surface reflectance, and a priori to the retrieval of aerosol extinction profile via sensitivity tests. The retrievals of the same Saharan dust profile used in Section 5.1 are performed here for the sensitivity tests. We perturb the SSA, AOD, surface reflectance, and a priori from the baseline retrieval in Section 5.1 and conduct the retrieval for each single perturbation. Figure 9a displays the results of the sensitivity tests for perturbing SSA, AOD, and surface reflectance at the whole spectra by $\pm 2\%$, $\pm 5\%$, and $\pm 10\%$, respectively. The values of the perturbation amplitudes were selected to produce discernible yet reasonable variations in the retrieval results, ensuring clarity in interpreting and presenting the relative sensitivities. With the perturbation of these parameters, the retrievals can still capture the general shape of the true profile. Table 3 displays the correlation coefficients

Table 3
Evaluation Metrics for Prior and Retrieved Aerosol Extinction Profiles in Sensitivity Tests

		R	RMSE (km ⁻¹)	MAE (km ⁻¹)
Baseline	<i>Pri. Baseline^a</i>	<i>0.891</i>	<i>0.225</i>	<i>0.164</i>
	Ret. Baseline	0.964	0.132	0.094
	SSA -2%	0.947	0.152	0.126
	SSA +2%	0.886	0.316	0.235
	AOD -5%	0.945	0.169	0.136
	AOD +5%	0.936	0.202	0.150
	Rs -10%	0.965	0.129	0.096
	Rs +10%	0.934	0.171	0.117
BL Peak	<i>Pri. BL Peak</i>	<i>0.561</i>	<i>0.775</i>	<i>0.612</i>
	Ret. BL Peak	0.760	0.248	0.139
FT Peak	<i>Pri. FT Peak</i>	<i>0.217</i>	<i>0.467</i>	<i>0.316</i>
	Ret. FT Peak	0.926	0.150	0.107

^aResults for prior aerosol vertical profiles are shown in italics.

(R), root mean square error (RMSE), and mean absolute error between the estimated aerosol extinction profiles and the ground truth across all layers below 6 km for the sensitivity tests. The variation of the aerosol profile retrievals is the largest with the lowest perturbation of the relative value of 2% for SSA, while the variation of the retrieval is the smallest with the largest perturbation of the relative value of 10% for surface reflectance. The impact of the AOD perturbation of 5% on the aerosol profile retrieval is slightly smaller than that of the SSA perturbation of 2%. The reason for that the uncertainty of surface reflectance has little impact on the aerosol profile retrieval is that the surface reflectance is low over the ocean surface (Table 1). This result demonstrates that the Lambertian ocean surface assumption would not affect the retrieval significantly. The performances of the retrievals over both land and ocean will be investigated using real satellite measurements in our part-2 study. We need to pay more attention to the SSA assumption in the retrieval since it brings the largest retrieval error.

Figure 9b presents the retrievals of the same dust extinction profile discussed in Section 5.1, using three different prior profiles. The baseline a priori (Pri. Baseline, red dashed line) is identical to the one used in the baseline retrieval (Figure 8d) in Section 5.1, which is derived from the local PC climatology based on the 15 years of CALIOP data. Therefore, the baseline a priori itself

already closely resembles the general shape of the ground truth. The other two prior profiles were designed to represent extreme scenarios in which the a priori significantly deviates from the ground truth in two different directions. The second a priori profile with a single aerosol extinction peak within the boundary layer (Pri. BL Peak, green dashed line) misses the elevated dust extinction peak at ~3 km, while the last a priori profile with the primary extinction peak in the free troposphere (Pri. FT Peak, blue dashed line) significantly underestimates the aerosol extinction peak near the surface. Table 3 presents the evaluation metrics for all prior and retrieved aerosol extinction profiles. All three retrievals exhibit a strong consistency with the ground truth profile, which indicates the robustness of the inversion algorithm. However, the final retrievals are still affected by the shape of the prior profiles. The baseline retrieval (Ret. Baseline, red solid line) achieves the highest accuracy and best agreement since its corresponding prior profile (Pri. Baseline) most closely resembles the true profile. The retrieval from Pri. BL Peak (Ret. BL Peak, green solid line) displays an aerosol extinction peak ~500 m higher than that of the ground truth profile within the marine boundary layer, a bias attributed to the similar vertical structure of Pri. BL Peak. The extinction peak near the surface in the retrieval from Pri. FT Peak (Ret. FT Peak, blue solid line) is ~0.5 km⁻¹ lower than the ground truth, which is caused by the significant underestimation of the surface peak by Pri. FT Peak.

6. Summary

This study developed an algorithm to retrieve the aerosol vertical profile from passive satellite sensors for hyperspectral measurements at UV, O₂-A, and O₂-B bands, such as TROPOMI and HiMAP. We built up a theoretical framework to represent the aerosol extinction profile with 3–5 most important EOFs and corresponding PC values, which are calculated from the PCA of 15 years of CALIOP measurements of regional aerosol vertical profiles. The retrieval algorithm is then simplified to derive 3–5 weighting coefficients of prescribed EOFs to reconstruct the aerosol extinction profile.

We applied an optimal inversion technique to retrieve the EOF weights based on the Jacobian calculation and L-BFGS-B algorithm (Byrd et al., 1995; Xiao & Zhang, 2008). A new PC module was developed in the radiative transfer model UNL-VRM (Wang et al., 2014) to represent the aerosol extinction profile with first 3–5 EOFs and compute the Jacobians of TOA reflectance with respect to EOF weights. The representativeness of the aerosol vertical profile is tested with three Saharan dust profiles in the newly developed PC module. The PCA method shows the advantage of capturing the multilayer structure of aerosol vertical distribution, surpassing the simple aerosol profile assumptions used in the previous studies (Chimot et al., 2018; Xu et al., 2019; Zeng et al., 2020). The analytical computation of Jacobians in the new PC module is validated against the central finite difference calculation, and they display good agreements.

The averaging kernel analysis shows that TROPOMI measurements cannot resolve the aerosol extinction layer by layer. The multiangle and polarimetric measurements at O₂-A and O₂-B bands from HiMAP with the spectral resolution twice as fine as TROPOMI measurements can resolve some of the aerosol vertical variations. However, some high aerosol loading features may be missed, and some false aerosol signals could be retained from the a priori. The PCA technique proposed by this study is necessary for a reasonable retrieval of the aerosol extinction profile using TROPOMI data, and HiMAP could potentially provide more information for retrieving aerosols in the lower part of the atmosphere. More studies are needed and planned to develop the HiMAP retrieval concept and algorithm.

Finally, we conducted the retrieval experiments for Saharan dust profiles using synthetic TROPOMI measurements. The retrieval of the dust profile case successfully captures the general shape of the ground truth with the elevated dust transport peaking at around 3 km and the other aerosol layer within the marine boundary layer, significantly improving the agreement with the ground truth profile. The error propagation analysis indicates that the uncertainty of the SSA assumption is the largest error source for the dust profile retrieval, while the impacts of surface reflectance uncertainty is minor because the ocean surface is quite dark. The impact of the AOD error on the aerosol profile retrieval is also important but smaller than that of SSA uncertainty. The sensitivity test using different prior profiles for the retrievals indicates the robustness of the inversion algorithm. The retrievals exhibit strong consistency with the true profile even if the prior profiles significantly deviate from the ground truth. However, the final retrievals are still affected by the shape of the prior profiles.

Conflict of Interest

The authors declare no conflicts of interest relevant to this study.

Data Availability Statement

CALIPOP Level 3 Tropospheric Aerosol Profile product is available at https://asdc.larc.nasa.gov/data/CALIPSO/LID_L3_Tropospheric_APro_CloudFree-Standard-V4-20/ and https://asdc.larc.nasa.gov/data/CALIPSO/LID_L3_Tropospheric_APro_CloudFree-Standard-V4-21/. The UNL-VRM model can be found at <https://unl-rtm.org>. All the codes (Lu, 2025a) used for the analysis and generation of the results presented in this paper can be accessed at <https://doi.org/10.5281/zenodo.17401671> and the data set (Lu, 2025b) used in this research can be found at <https://doi.org/10.5281/zenodo.17401846>.

Acknowledgments

This study is supported by the NASA MAIA project (JPL Grant: 1583456), remote sensing theory program (Grant: 80NSSC20K1747), TEMPO project (Smithsonian Institution Grant: SV7-87011), Instrument Incubator Program (Grant: 80NSSC25K7305), and NOAA GEO-XO project (Grant: NA23OAR4310303). The research was carried out at the Jet Propulsion Laboratory, California Institute of Technology, under a contract with the National Aeronautics and Space Administration (Grant: 80NM0018D0004).

References

- Babic, L., Braak, R., Dierssen, W., Kissi-Ameyaw, J., Kleipool, Q., Leloux, J., et al. (2022). Algorithm theoretical basis document for the TROPOMI L01b data processor. Retrieved from <https://sentinels.copernicus.eu/documents/247904/2476257/Sentinel-5P-TROPOMI-Level-1B-ATBD>
- Baldrige, A. M., Hook, S. J., Grove, C. I., & Rivera, G. (2009). The ASTER spectral library version 2.0. *Remote Sensing of Environment*, 113(4), 711–715. <https://doi.org/10.1016/j.rse.2008.11.007>
- Byrd, R. H., Lu, P. H., Nocedal, J., & Zhu, C. Y. (1995). A limited memory algorithm for bound constrained optimization. *SIAM Journal on Scientific Computing*, 16(5), 1190–1208. <https://doi.org/10.1137/0916069>
- Chen, X., Wang, J., Xu, X., Zhou, M., Zhang, H., Castro Garcia, L., et al. (2021a). First retrieval of absorbing aerosol height over dark target using TROPOMI oxygen B band: Algorithm development and application for surface particulate matter estimates. *Remote Sensing of Environment*, 265, 112674. <https://doi.org/10.1016/j.rse.2021.112674>
- Chen, X., Xu, X., Wang, J., & Diner, D. J. (2021b). Can multi-angular polarimetric measurements in the oxygen-A and B bands improve the retrieval of aerosol vertical distribution? *Journal of Quantitative Spectroscopy and Radiative Transfer*, 270, 107679. <https://doi.org/10.1016/j.jqsrt.2021.107679>
- Chew, B. N., Campbell, J. R., Salinas, S. V., Chang, C. W., Reid, J. S., Welton, E. J., et al. (2013). Aerosol particle vertical distributions and optical properties over Singapore. *Atmospheric Environment*, 79, 599–613. <https://doi.org/10.1016/j.atmosenv.2013.06.026>
- Chimot, J., Veefkind, J. P., Vlemmix, T., & Levelt, P. F. (2018). Spatial distribution analysis of the OMI aerosol layer height: A pixel-by-pixel comparison to CALIOP observations. *Atmospheric Measurement Techniques*, 11(4), 2257–2277. <https://doi.org/10.5194/amt-11-2257-2018>
- Choi, M., Sander, S. P., Spurr, R. J. D., Pongetti, T. J., van Harten, G., Drouin, B. J., et al. (2021). Aerosol profiling using radiometric and polarimetric spectral measurements in the O₂ near infrared bands: Estimation of information content and measurement uncertainties. *Remote Sensing of Environment*, 253, 112179. <https://doi.org/10.1016/j.rse.2020.112179>
- Colosimo, S. F., Natraj, V., Sander, S. P., & Stutz, J. (2016). A sensitivity study on the retrieval of aerosol vertical profiles using the oxygen A-band. *Atmospheric Measurement Techniques*, 9(4), 1889–1905. <https://doi.org/10.5194/amt-9-1889-2016>
- Diner, D. J., Boland, S. W., Brauer, M., Bruegge, C., Burke, K. A., Chipman, R., et al. (2018). Advances in multiangle satellite remote sensing of speciated airborne particulate matter and association with adverse health effects: From MISR to MAIA. *Journal of Applied Remote Sensing*, 12(4), 1. <https://doi.org/10.1117/1.Jrs.12.042603>
- Ding, S., Wang, J., & Xu, X. (2016). Polarimetric remote sensing in oxygen A and B bands: Sensitivity study and information content analysis for vertical profile of aerosols. *Atmospheric Measurement Techniques*, 9(5), 2077–2092. <https://doi.org/10.5194/amt-9-2077-2016>

- Ge, C., Wang, J., & Reid, J. S. (2014). Mesoscale modeling of smoke transport over the Southeast Asian maritime continent: Coupling of smoke direct radiative effect below and above the low-level clouds. *Atmospheric Chemistry and Physics*, *14*(1), 159–174. <https://doi.org/10.5194/acp-14-159-2014>
- Herman, J. R., Bhartia, P. K., Torres, O., Hsu, C., Sefstor, C., & Celarier, E. (1997). Global distribution of UV-absorbing aerosols from nimbus 7/TOMS data. *Journal of Geophysical Research*, *102*(D14), 16911–16922. <https://doi.org/10.1029/96jd03680>
- Hollstein, A., & Filipitsch, F. (2014). Global representation of aerosol vertical profiles by sums of lognormal modes: Consequences for the passive remote sensing of aerosol heights. *Journal of Geophysical Research-Atmospheres*, *119*(14), 8899–8907. <https://doi.org/10.1002/2014jd021472>
- Hou, W. Z., Wang, J., Xu, X. G., & Reid, J. S. (2017). An algorithm for hyperspectral remote sensing of aerosols: 2. Information content analysis for aerosol parameters and principal components of surface spectra. *Journal of Quantitative Spectroscopy and Radiative Transfer*, *192*, 14–29. <https://doi.org/10.1016/j.jqsrt.2017.01.041>
- Hou, W. Z., Wang, J., Xu, X. G., Reid, J. S., & Han, D. (2016). An algorithm for hyperspectral remote sensing of aerosols: 1. Development of theoretical framework. *Journal of Quantitative Spectroscopy and Radiative Transfer*, *178*, 400–415. <https://doi.org/10.1016/j.jqsrt.2016.01.019>
- Hou, W. Z., Wang, J., Xu, X. G., Reid, J. S., Janz, S. J., & Leitch, J. W. (2020). An algorithm for hyperspectral remote sensing of aerosols: 3. Application to the GEO-TASO data in KORUS-AQ field campaign. *Journal of Quantitative Spectroscopy and Radiative Transfer*, *253*, 107161. <https://doi.org/10.1016/j.jqsrt.2020.107161>
- Hsiao, H. H., Muller, R. E., McGuire, J. P., Nemchick, D. J., Shen, C. H., van Harten, G., et al. (2022). An ultra-broadband high efficiency polarization beam splitter for high spectral resolution polarimetric imaging in the near infrared. *Advanced Science*, *9*(27), 2201227. <https://doi.org/10.1002/advs.202201227>
- Hsu, N. C., Jeong, M. J., Bettenhausen, C., Sayer, A. M., Hansell, R., Sefstor, C. S., et al. (2013). Enhanced deep blue aerosol retrieval algorithm: The second generation. *Journal of Geophysical Research-Atmospheres*, *118*(16), 9296–9315. <https://doi.org/10.1002/jgrd.50712>
- Hsu, N. C., Tsay, S. C., King, M. D., & Herman, J. R. (2004). Aerosol properties over bright-reflecting source regions. *IEEE Transactions on Geoscience and Remote Sensing*, *42*(3), 557–569. <https://doi.org/10.1109/tgrs.2004.824067>
- Johnson, B. T., Shine, K. P., & Forster, P. M. (2004). The semi-direct aerosol effect: Impact of absorbing aerosols on marine stratocumulus. *Quarterly Journal of the Royal Meteorological Society*, *130*(599), 1407–1422. <https://doi.org/10.1256/qj.03.61>
- Joseph, J. H., Yaron, O., Yaroslavich, E., Israelevich, P., Koren, I., Yair, Y., et al. (2008). Determination of Most probable height of desert dust aerosol layer from space. *Journal of Geophysical Research*, *113*(D20), D20S93. <https://doi.org/10.1029/2007jd009646>
- Kahn, R. A., Chen, Y., Nelson, D. L., Leung, F. Y., Li, Q. B., Diner, D. J., & Logan, J. A. (2008). Wildfire smoke injection heights: Two perspectives from space. *Geophysical Research Letters*, *35*(4), L04809. <https://doi.org/10.1029/2007gl032165>
- Kaufman, Y. J., Tanre, D., Remer, L. A., Vermote, E. F., Chu, A., & Holben, B. N. (1997). Operational remote sensing of tropospheric aerosol over land from EOS moderate resolution imaging spectroradiometer. *Journal of Geophysical Research*, *102*(D14), 17051–17067. <https://doi.org/10.1029/96jd03988>
- Lee, J., Hsu, N. C., Sayer, A. M., Sefstor, C. J., & Kim, W. V. (2020). Aerosol layer height with enhanced spectral coverage achieved by synergy between VIIRS and OMPS-NM measurements. *IEEE Geoscience and Remote Sensing Letters*, *18*(6), 1–5. <https://doi.org/10.1109/lgrs.2020.2992099>
- Levy, R. C., Mattoo, S., Munchak, L. A., Remer, L. A., Sayer, A. M., Patadia, F., & Hsu, N. C. (2013). The collection 6 MODIS aerosol products over land and ocean. *Atmospheric Measurement Techniques*, *6*(11), 2989–3034. <https://doi.org/10.5194/amt-6-2989-2013>
- Levy, R. C., Remer, L. A., Mattoo, S., Vermote, E. F., & Kaufman, Y. J. (2007). Second-generation operational algorithm: Retrieval of aerosol properties over land from inversion of moderate resolution imaging spectroradiometer spectral reflectance. *Journal of Geophysical Research*, *112*(D13), D13211. <https://doi.org/10.1029/2006jd007811>
- Lu, Z. (2025a). Aerosol_Profile_Inversion_Code_part1 [Software]. Zenodo. <https://doi.org/10.5281/zenodo.17401671>
- Lu, Z. (2025b). Aerosol_Profile_Inversion_Data_Part1 [Dataset]. Zenodo. <https://doi.org/10.5281/zenodo.17401846>
- Lu, Z., Wang, J., Chen, X., Zeng, J., Wang, Y., Xu, X., et al. (2023). First mapping of monthly and diurnal climatology of Saharan dust layer height over the Atlantic Ocean from EPIC/DSCOVR in deep space. *Geophysical Research Letters*, *50*(5), e2022GL102552. <https://doi.org/10.1029/2022GL102552>
- Lu, Z., Wang, J., Xu, X., Chen, X., Kondragunta, S., Torres, O., et al. (2021). Hourly mapping of the layer height of thick smoke plumes over the Western U.S. in 2020 severe fire season. *Frontiers in Remote Sensing*, *2*, 766628. <https://doi.org/10.3389/frsen.2021.766628>
- Lyapustin, A., Wang, Y. J., Korkin, S., & Huang, D. (2018). MODIS collection 6 MAIAC algorithm. *Atmospheric Measurement Techniques*, *11*(10), 5741–5765. <https://doi.org/10.5194/amt-11-5741-2018>
- Meloni, D., di Sarra, A., Di Iorio, T., & Fiocco, G. (2005). Influence of the vertical profile of Saharan dust on the visible direct radiative forcing. *Journal of Quantitative Spectroscopy and Radiative Transfer*, *93*(4), 397–413. <https://doi.org/10.1016/j.jqsrt.2004.08.035>
- Mishra, A. K., Koren, I., & Rudich, Y. (2015). Effect of aerosol vertical distribution on aerosol-radiation interaction: A theoretical prospect. *Heliyon*, *1*(2), e00036. <https://doi.org/10.1016/j.heliyon.2015.e00036>
- Nanda, S., de Graaf, M., Veefkind, J. P., Sneep, M., ter Linden, M., Sun, J., & Levelt, P. F. (2020). A first comparison of TROPOMI aerosol layer height (ALH) to CALIOP data. *Atmospheric Measurement Techniques*, *13*(6), 3043–3059. <https://doi.org/10.5194/amt-13-3043-2020>
- Nanda, S., de Graaf, M., Veefkind, J. P., ter Linden, M., Sneep, M., de Haan, J., & Levelt, P. F. (2019). A neural network radiative transfer model approach applied to the tropospheric monitoring instrument aerosol height algorithm. *Atmospheric Measurement Techniques*, *12*(12), 6619–6634. <https://doi.org/10.5194/amt-12-6619-2019>
- Nelson, D. L., Garay, M. J., Kahn, R. A., & Dunst, B. A. (2013). Stereoscopic height and wind retrievals for aerosol plumes with the MISR Interactive eXplorer (MINX). *Remote Sensing*, *5*(9), 4593–4628. <https://doi.org/10.3390/rs5094593>
- Peyridieu, S., Chedin, A., Tanre, D., Capelle, V., Pierangelo, C., Lamquin, N., & Armante, R. (2010). Saharan dust infrared optical depth and altitude retrieved from AIRS: A focus over north Atlantic - Comparison to MODIS and CALIPSO. *Atmospheric Chemistry and Physics*, *10*(4), 1953–1967. <https://doi.org/10.5194/acp-10-1953-2010>
- Reid, J. S., Kuehn, R. E., Holz, R. E., Eloranta, E. W., Kaku, K. C., Kuang, S., et al. (2017). Ground-based high spectral resolution lidar observation of aerosol vertical distribution in the summertime southeast United States. *Journal of Geophysical Research: Atmospheres*, *122*(5), 2970–3004. <https://doi.org/10.1002/2016jd025798>
- Richter, J., Chipman, R., Daugherty, B., Diner, D. J., Eldering, A., Hyon, J. J., et al. (2019). Specifying Polarimetric Tolerances of a High-resolution Imaging Multiple-species Atmospheric Profiler (HiMAP) In. *Paper presented at the conference on photonic instrumentation engineering*. VI
- Rodgers, C. D. (2000). *Inverse methods for atmospheric sounding: Theory and practice*. World Scientific.
- Sawyer, V., Levy, R. C., Mattoo, S., Cureton, G., Shi, Y. X., & Remer, L. A. (2020). Continuing the MODIS dark target aerosol time series with VIIRS. *Remote Sensing*, *12*(2), 308. <https://doi.org/10.3390/rs12020308>

- Seo, S., Kim, J., Lee, H., Jeong, U., Kim, W., Holben, B. N., et al. (2015). Estimation of PM₁₀ concentrations over Seoul using multiple empirical models with AERONET and MODIS data collected during the DRAGON-Asia campaign. *Atmospheric Chemistry and Physics*, 15(1), 319–334. <https://doi.org/10.5194/acp-15-319-2015>
- Su, T. N., Li, Z. Q., Zheng, Y. T., Wu, T., Wu, H., & Guo, J. P. (2022). Aerosol-boundary layer interaction modulated entrainment process. *Npj Climate and Atmospheric Science*, 5(1), 64. <https://doi.org/10.1038/s41612-022-00283-1>
- Tilstra, L. G., de Graaf, M., Trees, V. J. H., Litvinov, P., Dubovik, O., & Stammes, P. (2024). A directional surface reflectance climatology determined from TROPOMI observations. *Atmospheric Measurement Techniques*, 17(7), 2235–2256. <https://doi.org/10.5194/amt-17-2235-2024>
- Torres, O., Bhartia, P. K., Herman, J. R., Ahmad, Z., & Gleason, J. (1998). Derivation of aerosol properties from satellite measurements of backscattered ultraviolet radiation: Theoretical basis. *Journal of Geophysical Research*, 103(D14), 17099–17110. <https://doi.org/10.1029/98jd00900>
- Val Martin, M., Heald, C. L., Ford, B., Prenni, A. J., & Wiedinmyer, C. (2013). A decadal satellite analysis of the origins and impacts of smoke in Colorado. *Atmospheric Chemistry and Physics*, 13(15), 7429–7439. <https://doi.org/10.5194/acp-13-7429-2013>
- Vandenbussche, S., Kochenova, S., Vandaele, A. C., Kumps, N., & De Maziere, M. (2013). Retrieval of desert dust aerosol vertical profiles from IASI measurements in the TIR atmospheric window. *Atmospheric Measurement Techniques*, 6(10), 2577–2591. <https://doi.org/10.5194/amt-6-2577-2013>
- Vasilkov, A., Lyapustin, A., Mitchell, B. G., & Huang, D. (2019). UV reflectance of the ocean from DSCOVR/EPIC: Comparisons with a theoretical model and Aura/OMI observations. *Journal of Atmospheric and Oceanic Technology*, 36(11), 2087–2099. <https://doi.org/10.1175/jtech-d-18-0150.1>
- Wang, J., & Christopher, S. A. (2006). Mesoscale modeling of Central American smoke transport to the United States: 2. Smoke radiative impact on regional surface energy budget and boundary layer evolution. *Journal of Geophysical Research*, 111(D14), D14S92. <https://doi.org/10.1029/2005jd006720>
- Wang, J., Christopher, S. A., Nair, U. S., Reid, J. S., Prins, E. M., Szykman, J., & Hand, J. L. (2006). Mesoscale modeling of Central American smoke transport to the United States: 1. “Top-down” assessment of emission strength and diurnal variation impacts. *Journal of Geophysical Research*, 111(D5), D05S17. <https://doi.org/10.1029/2005jd006416>
- Wang, J., Xu, X., Ding, S., Zeng, J., Spurr, R., Liu, X., et al. (2014). A numerical testbed for remote sensing of aerosols, and its demonstration for evaluating retrieval synergy from a geostationary satellite constellation of GEO-CAPE and GOES-R. *Journal of Quantitative Spectroscopy and Radiative Transfer*, 146, 510–528. <https://doi.org/10.1016/j.jqsrt.2014.03.020>
- Wilcox, E. M. (2012). Direct and semi-direct radiative forcing of smoke aerosols over clouds. *Atmospheric Chemistry and Physics*, 12(1), 139–149. <https://doi.org/10.5194/acp-12-139-2012>
- Winker, D. M., Tackett, J. L., Getzewich, B. J., Liu, Z., Vaughan, M. A., & Rogers, R. R. (2013). The global 3-D distribution of tropospheric aerosols as characterized by CALIOP. *Atmospheric Chemistry and Physics*, 13(6), 3345–3361. <https://doi.org/10.5194/acp-13-3345-2013>
- Winker, D. M., Vaughan, M. A., Omar, A., Hu, Y. X., Powell, K. A., Liu, Z. Y., et al. (2009). Overview of the CALIPSO mission and CALIOP data processing algorithms. *Journal of Atmospheric and Oceanic Technology*, 26(11), 2310–2323. <https://doi.org/10.1175/2009jtecha1281.1>
- Worden, J., Liu, X., Bowman, K., Chance, K., Beer, R., Eldering, A., et al. (2007). Improved tropospheric ozone profile retrievals using OMI and TES radiances. *Geophysical Research Letters*, 34(1), L01809. <https://doi.org/10.1029/2006gl027806>
- Wu, L., Hasekamp, O., van Diedenhoven, B., Cairns, B., Yorks, J. E., & Chowdhary, J. (2016). Passive remote sensing of aerosol layer height using near-UV multiangle polarization measurements. *Geophysical Research Letters*, 43(16), 8783–8790. <https://doi.org/10.1002/2016GL069848>
- Xiao, Y. H., & Zhang, H. C. (2008). Modified subspace limited memory BFGS algorithm for large-scale bound constrained optimization. *Journal of Computational and Applied Mathematics*, 222(2), 429–439. <https://doi.org/10.1016/j.cam.2007.11.014>
- Xu, X., Wang, J., Wang, Y., & Kokhanovsky, A. (2018). Passive remote sensing of aerosol height. In *Remote sensing of aerosols, clouds, and precipitation* (pp. 1–22). Elsevier.
- Xu, X., Wang, J., Wang, Y., Zeng, J., Torres, O., Reid, J. S., et al. (2019). Detecting layer height of smoke aerosols over vegetated land and water surfaces via oxygen absorption bands: Hourly results from EPIC/DSCOVR in deep space. *Atmospheric Measurement Techniques*, 12(6), 3269–3288. <https://doi.org/10.5194/amt-12-3269-2019>
- Xu, X., Wang, J., Wang, Y., Zeng, J., Torres, O., Yang, Y., et al. (2017). Passive remote sensing of altitude and optical depth of dust plumes using the oxygen A and B bands: First results from EPIC/DSCOVR at Lagrange-1 point. *Geophysical Research Letters*, 44(14), 7544–7554. <https://doi.org/10.1002/2017gl073939>
- Zarzycki, C. M., & Bond, T. C. (2010). How much can the vertical distribution of Black carbon affect its global direct radiative forcing? *Geophysical Research Letters*, 37(20), L20807. <https://doi.org/10.1029/2010gl044555>
- Zeng, Z. C., Chen, S., Natraj, V., Le, T., Xu, F., Merrelli, A., et al. (2020). Constraining the vertical distribution of coastal dust aerosol using OCO-2 O₂ A-band measurements. *Remote Sensing of Environment*, 236, 14. <https://doi.org/10.1016/j.rse.2019.111494>
- Zhang, L., Li, Q. B., Gu, Y., Liou, K. N., & Meland, B. (2013). Dust vertical profile impact on global radiative forcing estimation using a coupled chemical-transport-radiative-transfer model. *Atmospheric Chemistry and Physics*, 13(14), 7097–7114. <https://doi.org/10.5194/acp-13-7097-2013>